Diagnostics of Magnetron Sputtering Discharges by Resonant Absorption Spectroscopy

Nikolay Britun, Stephanos Konstantinidis and Rony Snyders

Abstract

The determination of the absolute number density of species in gaseous discharge is one of the most important plasma diagnostics tasks. This information is especially demanded in the case of low-temperature sputtering discharges since the time- and space-resolved behavior of the sputtered particles in the ground state determines the plasma kinetics and plasma chemistry in this case. Historically, magnetron sputtering is often implied when talking about sputtering discharges due to the popularity and the numerous advantages this technique provides for coating applications. The determination of the absolute density of various atomic and molecular species in magnetron sputtering discharges along with its time and space evolution may be important from several points of view, since it may help to estimate the total flux of particles to a virtual surface in the plasma reactor, to compare the throughputs of two different sputtering systems, to use the absolute particle concentrations as an input data for discharge modeling, etc. This chapter is intended to provide an overview on the advantages and main principles of resonant absorption spectroscopy technique as a reliable tool for in situ diagnostics of the particle density, as well as on the recent progress in characterization of magnetron sputtering discharges using this technique, when the role of reference source is played by another low-temperature discharge. Both continuous and pulsed magnetron sputtering discharges are overviewed. Along with the introduction covering the main principles of magnetron sputtering, the description of the basics of resonant absorption technique, and the selected results related to the particle density determination in direct current and high-power pulsed magnetron sputtering discharges are given, covering both space- and time-resolved density evolutions.

Keywords: Magnetron sputtering, resonant optical absorption spectroscopy, ROAS, atomic absorption, absolute number density

1. Introduction: Magnetron sputtering discharges

Among the families of plasma-related methods involved in thin films growth, those belonging to physical vapor deposition (PVD) are among the most commonly utilized. The PVD-related techniques cover wide range of the deposition methods, including evaporation, vacuum arc deposition, laser ablation, and sputtering. These methods are different from another class referred to as chemical vapor deposition (CVD) in the sense that the source of material is solid or liquid as opposed to a gaseous one in the case of CVD [1]. Thermal evaporation has been the most used PVD process for many years because of the easy handling and relatively high deposition rate comparing to the first known sputtering process, namely, the diode sputtering [2]. The latter process has been known since its first description in 1852 by W. R. Grove, who had performed sputtering using a massive inductive coil [3]. In diode sputtering, ions of the sputter gas, commonly argon, hit a negatively biased cathode (also known as target) with energy up to several hundred electron volts (eV). This energy is high enough to induce ejection of the superficial atoms, which is followed by their condensation on the chamber surfaces, including a potential substrate [4]. In diode sputtering, however, due to the relatively high process pressure needed to ensure the discharge stability (nearly 0.1 Torr), the mean free path of the ejected atoms is in the mm range, which is much lower than the typical substrate-target distance (cm range) resulting in relatively poor quality of the deposited coating.

The limitations of diode sputtering have been overcome in 196× with the works of E. Kay and W. Gill [5,6], who have proposed to utilize magnetic field to create efficient electron trapping above the cathode (target) in order to accelerate the ionization and sputtering itself. The electron trapping region is created due to the fact that the electrons propagate mainly along the magnetic field lines as a result of well-known gyration effect (with gyration radius being in the μm range). The implementation of magnetic field for sputtering, naturally producing the name "magnetron," has been shortly followed by the introduction of planar magnetron sources in 1974 [2,7], for which the presence of permanent magnets beneath the cathode was a distinctive feature, as schematically illustrated in Figure 1. As a result of the electron trapping, these innovations led to essential increase in the ionization degree of the sputter (bulk) gas in the cathode vicinity. As a result, the pressure necessary to maintain the discharge current in this case could be reduced by about one order of magnitude, i.e., down to the mTorr range [5]. Another critical point related to efficiency of magnetron sputtering is the topology of magnetic field. Indeed, the arrangement of magnets beneath the cathode affects significantly the degree of electron confinement above the target. In the so-called balanced magnetron sources, the dense plasma region above the target is roughly comparable to its radius (assuming a planar circular target) [8]. If the substrate is located outside this region, the bombardment of growing film by the plasma ions is essentially reduced (the resulting ion current is <1 mA/cm^2), limiting the benefit of the sputtering process. This effect is different in the so-called unbalanced sources, where the topology of the magnetic field near cathode is different, letting some magnetic field lines reach the substrate. In this case, plasma is not confined completely, and the ion current densities of about 2–10 mA/cm^2 can be reached, which is typically one order of magnitude higher than in the case of balanced magnetrons [9].
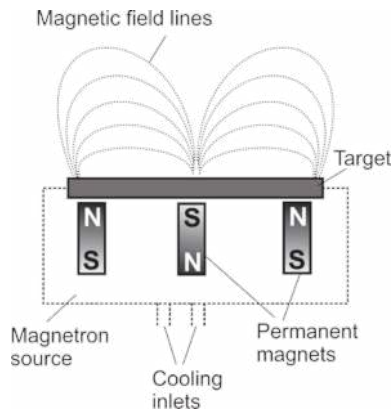
Figure 1. Side view of a typical magnetron source, including planar circular magnetron target, permanent magnets, and cooling system. The magnetic field lines are shown schematically.

In addition to magnetic field configuration, the voltage waveform and its repetition rate also play significant role in magnetron sputtering. The development of the plasma sources utilizing this effect has been mainly driven by the efficient deposition of the insulating compounds using reactive sputtering (see below). Thus, in addition to the well-known direct current magnetron sputtering (DCMS) devices, the radio frequency (RF) magnetron sources mainly working at 13.56 MHz have been introduced. Following the same trend, in the early 1990s, the idea of using pulsed-DCMS (also known as P-DCMS, or pulsed-DC) has been proposed (see, e.g., [10,11]). In most cases, the pulsed-DC power supplies operate successively alternating the negative (sputtering phase) and positive (charge dissipation phase) voltage cycles. The power supply in this case might be unipolar or bipolar, depending on polarity of the utilized pulses. Nowadays, most of magnetron sputtering processes for the synthesis of insulating compound coatings use pulsed magnetron sputtering approach [9].

Further development of the pulsed magnetron sputtering technology has triggered the new family of magnetron sputtering processes, so-called ionized physical vapor deposition (IPVD) techniques [12]. In a typical IPVD discharge, significant fraction of the sputtered atoms is ionized, reaching up to 100% in certain cases. The main idea behind the IPVD techniques is to generate denser plasmas than those appear in conventional magnetron sputtering in order to ionize the sputtered atoms more efficiently (up to the level of number densities $\sim 10^{13}$–10^{14} cm^{-3} vs. 10^{8}–10^{11} cm^{-3} in the DCMS case). Among the different approaches targeted to increase the ionization degree, such as using an inductive coil [13], or hollow cathodes [14], the high-power impulse magnetron sputtering technique, or HiPIMS (also known as high-power pulsed magnetron sputtering—HPPMS), is the most notorious IPVD example. HiPIMS discharge uses the pulse duration ranged from few μs to few hundreds μs, while the pulse repetition frequency typically varies from ~ 10 Hz to ~ 10 kHz. Under these conditions, the peak current density may reach values of up to several A/cm^{-2} compared to a few mA/cm^{-2} in DCMS, but only during a short time, typically 1–2% of the repetition period [15]. As a result, a dense plasma is generated during the plasma on time enabling not only efficient target sputtering but also high ionization degree

of metallic vapor [16], at the same time keeping the average applied power comparable to that of DCMS [15–17]. The schematic comparison of the DCMS, P-DCMS, and HiPIMS techniques in terms of the applied power is shown in Figure 2. Note that the level of time-averaged power applied to the sputtered cathode in each case is roughly the same, which is first of all due to the fact that the permanent magnets beneath the target should not be overheated and reach the Curie temperature (which is as low as about 580 K for widely used neodymium-based magnets). The actual applied power level is typically equal to several hundred Watt and often defined by the magnetron source cooling system (i.e., water temperature) used beneath the target. The interest to the pulsed magnetron discharges and, namely, the HiPIMS discharges from both scientific and application points of view has been continuously increasing since the introduction these techniques [18,19]. The main advantages of the HiPIMS technique, along with the achievements in characterization of these discharges, are described in the numerous works [15, 17,20–23].
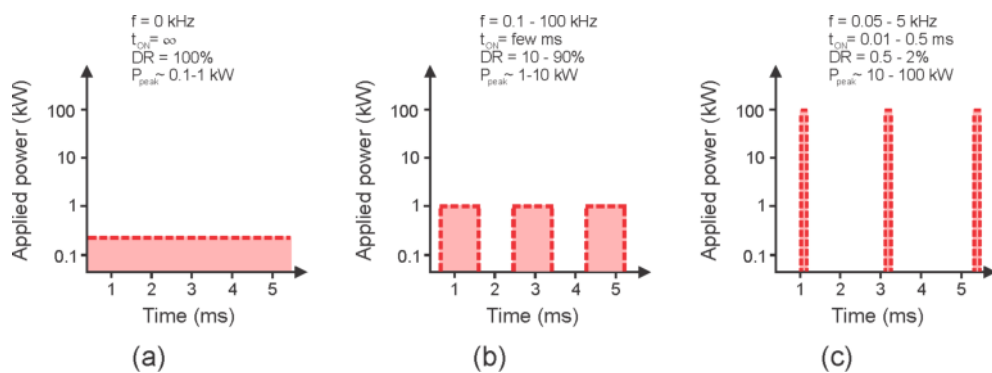

Figure 2. Comparison between the DCMS (a), P-DCMS (b), and HiPIMS (c) magnetron sputtering techniques in terms of the temporal distribution of the applied power. Typical range of the relevant discharge parameters and the values along both horizontal and vertical axes are given for reference only. The quantities f, t_{ON}, DR, and P_{peak} stand for repetition frequency, plasma on time, duty ratio, and peak power, respectively.

Why is the knowledge of the absolute density in plasma and particularly in magnetron sputtering discharges important? There are few main reasons making this parameter critical. First, *particle fluxes* in the discharge can be estimated knowing the density and velocity of each sort of the sputtered species, which is critical for any film growth process. Second, the discharge physics and chemistry can be significantly clarified having the absolute concentration of the relevant species in the discharge estimated properly. Third, the absolute concentration of the discharge species or their fluxes can be used as input information for further kinetic/chemical modeling of the discharge processes. Among the known plasma characterization approaches, resonant optical absorption spectroscopy (ROAS), also known as atomic absorption spectroscopy (AAS) [24,25], represents one of the straightforward ways for the determination of the absolute density of atomic and/or molecular species in gaseous discharges. Utilizing this technique, the density of the absorbers can be determined using an external (reference) light source by measuring the attenuation in its intensity after passing a volume with the absorbing

species (see, e.g., Mitchell and Zemansky [24], p. 92). Along with the laser-based plasma diagnostic techniques, such as laser-induced fluorescence (LIF), ROAS technique has been playing a significant role in studying the plasma discharges during the last decades, involving both coherent (such as diode lasers) [26–28], and noncoherent (e.g., hollow cathode lamps— HCL) [29–31] radiation sources. The range of applications of this technique has been continuously increasing due particularly to the improvements of the tunable diode laser systems, namely, their stability, power level, tuning range, etc. [27,32].

In the domain of magnetron sputtering discharges, the determination of number density of the discharge particles by ROAS has been undertaken in the variety of systems, including time-resolved [33] and space-resolved [34] characterization. In particular, among the recent achievements, the works of various research groups devoted to absolute density of sputtered atoms in the DCMS discharges [31,34,35], including those amplified by an RF coil [30], as well as the works of devoted to flux measurements in DCMS [36], should be mentioned. What is related to the utilization of ROAS in the HiPIMS domain, the works dealing with the determination of time-resolved absorption line profile [33], which have been realized using tunable diode laser absorption spectroscopy (TD-LAS), should be emphasized. In addition, a detailed time evolution of the Ar metastable $1s_5$ states (Ar^{met}) has been investigated in a long-pulsed (200 μs) HiPIMS discharge by Vitelaru et al. [26], where the Ar^{met} density growth, followed by its rarefication after about 50 μs, and a gradual refill afterward have been clearly demonstrated. These results are generally in a good agreement with the recent studies in HiPIMS involving LIF [37] and ROAS [38] techniques, which are partially overviewed here. The last two works ([37,38]) are devoted to the short-pulsed HiPIMS discharges studying the propagation of the ground state and metastable sputtered particles, being mainly targeted to the systematic time-resolved characterization of HIPIMS discharges in terms of absolute density of species, 2-D imaging of the main atomic states corresponding to the studied discharge species (LIF+ROAS), as well as to the study of several optically available energy states of the discharge species and their sublevels.

Unifying the recent achievements in the domain of the absolute density measurements for two "extreme" magnetron sputtering cases, namely, DCMS and HiPIMS, this chapter is mainly focused on the particularities of the mentioned sputtering discharges in terms of the absolute density of species where resonant absorption is used as a main diagnostics technique. The resonant absorption method overviewed in this chapter is considered as a reliable tool for the determination of the absolute density of species in the discharge volume and for understanding the sputtering processes at the atomic level.

2. Particularities of resonant absorption

The main principles of the resonant absorption are described in details in the work of Mitchell and Zemansky [24]. This method is based on resonant absorption of radiation emitted by a reference source and absorbed (by atoms or molecules) in an optically thin gaseous discharge. At a definite spectral line the absolute density of states corresponding to a lower level of a

chosen spectral transition can be determined by measuring so-called line absorption, i.e., an integral under spectral absorption line of interest, if the effective absorption lengths as well as the line width of both plasma and source spectral lines are known. This approach can be applied for the case when the spectral lines in the discharge are Doppler-limited [31], as well as can be generalized for more general cases [39]. The biggest advantage of ROAS technique is its nonintrusiveness. In this regard, this technique is different from the other methods used for density determination, which are based on the introduction of additional gases to the discharge (such as titration [40]), which may potentially change the electron energy distribution and the discharge kinetics. In addition, the fact ROAS uses external source of radiation and does not depend on the discharge emission itself is critical for characterization of the pulsed discharges, such as HiPIMS, especially during the afterglow time when optical emission spectroscopy (OES), cannot be applied.

As mentioned above, ROAS can be implemented in two different ways, namely, using a gaseous discharge emitting the spectral lines of interest, as well as using a monochromatic laser (e.g., a continuous tunable laser diode). Despite the fact that the laser-based diagnostics has several advantages [21,33], the discharge-based ROAS should be implemented. Among the main reasons for this are the following: (i) discharge-based ROAS setup is normally less expensive than the one based on a tunable laser; (ii) discharge-based ROAS depends on the line width ratio between the plasma and the reference source, which can be easily taken into account [24]; (iii) several spectral transitions can be studied in parallel in this case, as far as the emitters in the reference source coincide with the absorbers of interest, which is not possible with a monochromatic laser; and (iv) in case of a large spectral separation (few nm) between the lines of interest, laser-based absorption setup requires separate laser diodes for each transition, which involves additional calibration procedures. Due to the mentioned advantages, for example, the absolute density at the energy sublevels corresponding to a certain electronic state can be probed in a straightforward way, by simply following the changes in the emission intensity of the corresponding peaks from the reference source, as performed in the numerous studies [30,31,34,35,39]. Let us consider the main relations necessary to understand the ROAS method.

2.1. The basics of resonant absorption method

This chapter deals with the classical ROAS method described by Mitchell and Zemansky [24]. In the case of temperature-limited emission (absorption) lines in the reference source (and in the studied discharge), the application of the resonant absorption method is rather straightforward, and the details of its implementation in magnetron discharges can be found elsewhere [35,38]. In this section, only the essential relations important for understanding the absolute density determination using ROAS method are given. The number density of the absorbing species in the lower (often ground) state can be determined using the following relation:

$$N_{abs} = 1.2 \cdot 10^{12} k_0 \frac{\delta \sigma^p}{f_{ji}}, \tag{1}$$

where N_{abs} (cm^{-3}) is the absolute number density of the absorbing species in the lower state, k_0 (cm^{-1}) is the absorption coefficient corresponding to the center of the absorption line, $\delta\sigma^{\,p}$ (cm^{-1}) is the full width at half maximum (FWHM) of the plasma emission line, $f_{\,ji}$ is the absorption oscillator strength, and j (i) stands for lower (upper) level of a chosen transition, respectively. $f_{\,ji}$ can be found using the relation [41]:

$$f_{ji} = 1.5 \cdot 10^{-14} \frac{g_i}{g_j} A_{ij} \lambda_{ij}^2,$$ (2)

where g is the statistical weight of the corresponding energy level, A_{ij} is the emission proba-bility corresponding to $i \rightarrow j$ transition, and λ_{ij} is the transition wavelength.

The absorption coefficient k_0 in Eq. (1) can be determined based on measurements of line absorption A_L, representing the integral under the absorption line profile. In the case of Doppler broadening of the source emission and plasma absorption lines, A_L can be expressed as follows [34,39]:

$$A_L = \frac{2}{\sqrt{\pi}} \int_0^\infty \mathrm{Exp}\left(-x^2\right)\left(1 - \mathrm{Exp}\left(-k_0 L \cdot \mathrm{Exp}\left(-\alpha^2 x^2\right)\right)\right)dx,$$ (3)

where L is the effective absorption length (~30 cm in our case), and α is the reference source-to-plasma line broadenings ratio. In the Doppler-limited case $\alpha^2 = T_S / T_P$, where T_S and T_P are the absolute gas temperatures in the reference source and in the plasma, respectively. A_L is normally determined experimentally by measuring the intensities of the corresponding emission lines:

$$A_L = 1 - \frac{\text{transmitted radiation}}{\text{incident radiation}} = 1 - \frac{I_{PS} - I_P}{I_S},$$ (4)

where I_S is the light intensity from the reference source, I_P is the light intensity from the plasma, and I_{PS} is the (partially absorbed) light from the reference source passing through absorption region, along with the light from plasma, if any. The physical meaning of these quantities is illustrated in Figure 3.

After the experimental determination of line absorption A_L, according to Eq. (4), the absorption coefficient k_0 can be found as a result of solution of Eq. (3). This leads to a direct determination (according to Eq. (1)) of the absolute density of species corresponding to the lower atomic (molecular) state of a chosen spectral transition, if the effective absorption length L, as well as the oscillator strength $f_{\,ji}$ are known. The critical role in the determination of the absorption
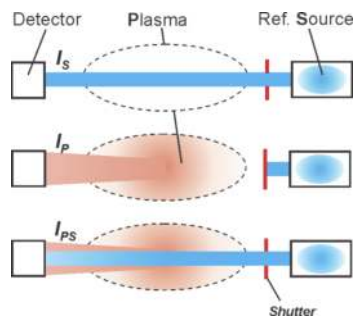
Figure 3. Schematic illustration of the absorption technique and the physical meaning of the quantities I_P, I_S, and I_{PS}.

coefficient is played by the coefficient α, representing the line broadening ratio of the spectral lines, as explained below.

2.2. Role of spectral line broadening

Several important remarks on the line broadening of plasma and reference source spectral lines should be made for proper interpretation of ROAS data. As mentioned above, this chapter deals with discharge-based ROAS when an HCL is primarily used as reference source. Since the gas pressure in HCL normally exceeds few Torr, and the mean free path of the gas particles is in the μm-range, the total particle thermalization can be assumed. The temperature in HCLs under the reviewed conditions, additionally measured by a high-resolution planar Fabry–Perot interferometer [42], is in the range of about 700–1100 K (see Table 1). Despite much lower pressure (~20–30 mTorr) in the magnetron discharges considered here (Table 1), similar considerations are also valid for the *bulk gas* atoms (Ar) in the studied DCMS and HiPIMS cases, which can be considered quasi-thermalized. The Ar temperature can be often assumed to be in the range of 300–500 K in this case, depending on the discharge type and its conditions [21,30,35,43].

Parameter	Value	Comment
DCMS system parameters		
Target	99.99% Ti	With water cooling
Target diameter/thickness	5 cm/0.5 cm	10 cm/1 cm for Figure 9
Working gas	99.999% Ar	
Working pressure	20 mTorr	30 mTorr for Figure 9
Base pressure	~10^{-6} Torr or less	
Time-averaged power	~200 W	500 W for Figure 9
Monocromator used	Princeton Instrument SpectraPro-500i	Jobin-Yvon HR-460 for Figure 9

Parameter	Value	Comment
Monocromator slit width	10 μm	
Spectral resolution	0.05 nm	
Optical detector used	Princeton Instrument PI-MAX ICCD	Hamamatsu R928 photomultiplier tube
HiPIMS system parameters		
Target	99.99% Ti	With water cooling
Target diameter/thickness	10 cm/1 cm	
Working gas	99.999% Ar	
Working pressure	20 mTorr	
Base pressure	$<10^{-6}$ Torr	
pulse duration/frequency	20 μs/1 kHz	Unless stated otherwise
Supplied energy per pulse(at 20 μs pulse)	≈0.26 J	Corresponding to ~260 W of time-averaged power
Monocromator used	Andor Shamrock 750	
Monocromator slit width	20–100 μm	
Spectral resolution	0.04–0.1 nm typically	
Optical detector used	Andor iStar DH740-18F ICCD	With ~10^3 pulses averaged
Resonant absorption parameters		
Beam diameter	≈1 cm	
Distance above the target, z	≈5 cm	$z = 0..10$ cm for Figure 8, $z = 8$ cm for Figure 9.
Effective absorption length, L	30 cm	Variable for Figure 8, L=25 cm for Figure 9.
Reference source type	Ar-Ba and Ne-Ti hollow cathode lamps	
Reference source pulse duration	40–100 μs	Continuous for Figure 8, 150 μs for Figure 9.
Reference source temperature	≈1100 K (in pulsed mode [38])	950 K for Figure 8 [34], 630 K for Figure 9 [54].
DCMS plasma temperature	580 K (Figure 8), 300 K (Figure 9)	
HiPIMS plasma temperature (Ar)	≈500 K	Based on OES measurements [43]
HiPIMS plasma line width (Ti)	≈5.5 GHz	Based on LIF measurements [44]

Table 1. Main parameters of the DCMS and HiPIMS discharges described in this work and characterized by resonant optical absorption spectroscopy.

The broadening of spectral lines corresponding to the *sputtered* particles may differ from those of the bulk gas (Ar), however. In the DCMS case, despite the fact the sputtered particles are far from thermalization, their velocity distribution function (VDF) can be often approximated by a Gaussian profile. This VDF does not change in time, by definition of DCMS discharge [37], and often can be associated with the particle temperature in the range of 300–700 K for the conditions described here (see Table 1). Due to the directional motion of the sputtered particles in magnetron plasma, the spectral line in the direction of measurements (i.e., along the ROAS line-of-sight) might be significantly broadened, as compared to the one of the reference source. This situation is schematically illustrated in Figure 4. In this case, the resonant absorption will happen only for a part of the total line width, and the ratio between the mentioned broadenings has to be introduced ($\delta\sigma^S/\delta\sigma^P$) to take into account the broadening difference, as described in details by Mitchell and Zemansky [24]. The similar approach should also be utilized in case non-Doppler line broadening dominates in the discharge, as studied recently by Li et al. [39].
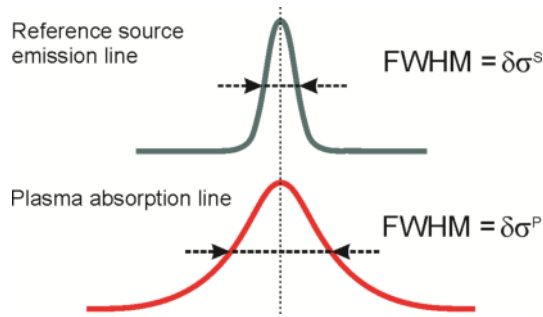

Reference source
emission line
$\text{FWHM} = \delta\sigma^S$

Plasma absorption line
$\text{FWHM} = \delta\sigma^P$

Figure 4. Illustration of the spectral line broadening (FWHM) of the reference source (emission) and plasma (absorption) lines along with their broadening notations.

The situation is yet different for HiPIMS discharges, which are far from thermalization during the plasma on time, especially in the target vicinity [37,43]. The distribution of the velocity component parallel to the target ($v_{||}$) in this case is often different from the Maxwell–Boltzmann one (even though it still can be roughly fitted by a Gaussian profile [33]), and the gas temperature in the classic sense cannot be applied. Because of this, the VDF line width corresponding to a particular velocity component and defining the line width of the emission (absorption) line should be determined separately. The dynamics of the line broadening in HiPIMS has been studied recently by LIF [44,45]. Based on these works, under the conditions described here (20 mTorr, $z = 5$ cm), the VDF width changes only by about 25%, which has rather minor impact on the final density of absorbers determined by Eq. (1). Due to this fact, the plasma absorption line width is assumed constant during the whole HiPIMS discharge period for simplicity, as described in [38,44] (see Table 1). These assumptions are additionally justified by the fact that the absorption coefficient k_0, determined based on Eq. (3) is weakly dependent on the plasma line width $\delta\sigma^P$.

2.3. Experimental setup for resonant absorption

The typical experimental arrangement for characterization of magnetron sputtering discharge by resonant spectroscopy is shown in Figure 5. The main parameters related to the discharges overviewed in this work are summarized in Table 1. Both in DCMS and HiPIMS cases, a cylindrical vacuum chamber with either horizontally or vertically placed balanced magnetron sputtering source holding a planar circular magnetron target has been used. The Ti magnetron targets, 5 or 10 cm in diameter, attached to a magnet-supporting water-cooled copper base, have been utilized. The commercial power supplies have been used to sustain the DCMS discharges, as described elsewhere [30,34]. In the HiPIMS case, the discharge current and voltage along with the pulse parameters have been controlled by the Lab.-made power supply, described by Ganciu et al. [46]. The HiPIMS discharge typically had 20 μs of the pulse duration and 1 kHz of the repetition frequency (thus having 980 μs of the plasma off time). The typical current–voltage waveforms can be found elsewhere [43,44,47]. The base pressure in the magnetron reactor has been kept $<10^{-6}$ Torr, whereas the bulk gas (99.999% Ar) pressure was normally fixed at 20 mTorr during all the ROAS measurements, unless stated otherwise. In order to avoid deposition on the quartz window surface, the special collimators (Ni tubes) with high length-to-radius ratio have been installed in front of each viewport inside the reactor.
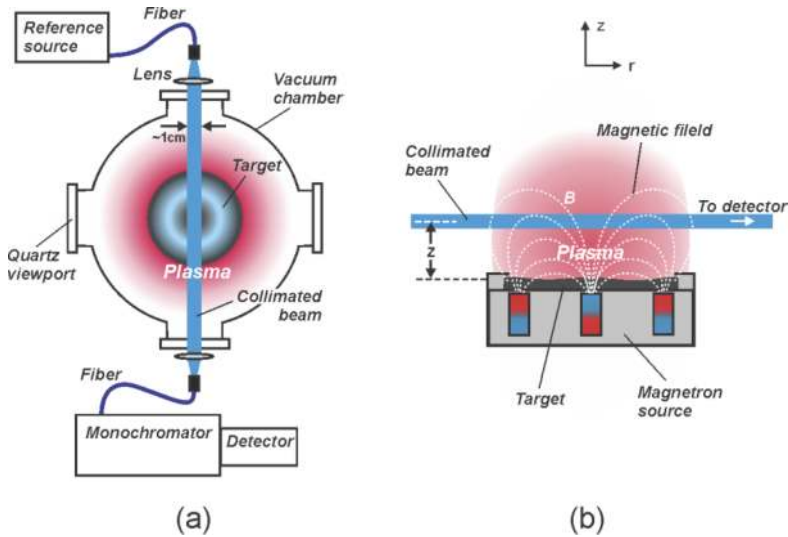

Figure 5. Top (a) and side (b) view of the experimental setup utilized for absolute density measurements in a magnetron sputtering discharge by ROAS. Role of the reference source is played by a hollow cathode lamp. Reproduced with permission from Britun et al. [38]. Copyright 2015 AIP Publishing.

The Perkin Elmer hollow cathode lamps (one with Ti cathode filled by Ne, and another one with Ba cathode filled by Ar) have been used as the reference sources. The HCLs have been running either in the continuous or pulsed regime (mainly in the HiPIMS case) in order to increase the emission intensity and make it comparable with the HiPIMS plasma emission,

aiming at reducing the measurements error during the plasma on time [43,48]. Apart from this, the pulse regime of HCL source favors the ionization of the cathode material inside the lamp, which is critical for analysis of the Ti^+ states [30]. During the measurements, the HCLs have a pulse duration typically ranging from 40 to 100 µs. About 10^3 pulses from the reference source have been averaged by the detector during the measurements of the absorption coefficient. The HCL pulse sequence was triggered by the HiPIMS power supply using the external transistor-transistor logic (TTL) trigger and was time shifted relatively to the HiPIMS plasma pulse using an additional analog TGP-110 pulse generator.

In some cases, when the density of absorbers in the studied discharge is too low, an improved detection scheme, including a triple optical fiber and allowing simultaneous acquisition of the I_S, I_P, and I_{PS} signals, may significantly increase the reliability of the obtained data. Such a scheme, illustrated in Figure 6, allows to avoid the instabilities of the plasma discharge and/or of the reference source during the acquisition time (which may last for several minutes) because the signals necessary to calculate the line absorption are taken simultaneously in this case, as described by Britun et al. [48]. The diagnostics setup in this case contains a reference emission source, a multichannel optical fiber, a group of lenses for beam collimation before passing the vacuum chamber, and a monochromator with an optical detector, according to Figure 5(a).
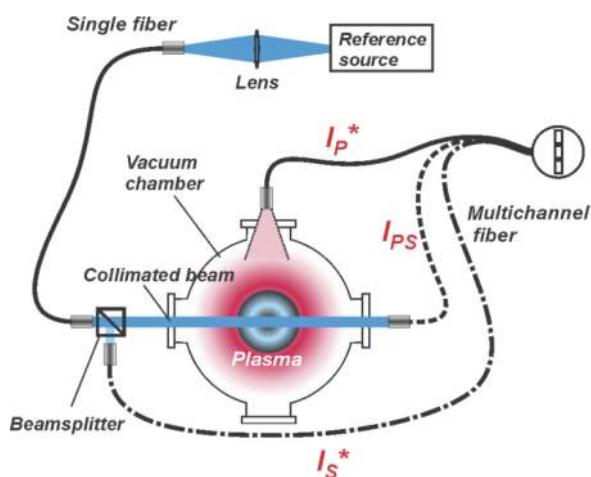

Figure 6. Scheme of the experimental setup for absorption measurements with increased reliability utilizing simultaneous acquisition of the plasma and source optical signals (I_P, I_S, and I_{PS}) necessary for calculation of the line absorption A_L.

A monochromator equipped with an intensified charge-coupled device (ICCD) camera and connected to the discharge reactor by an optical fiber has been used for spectral acquisition in most cases. The spectral resolution of the monochromator was typically ≈0.05–0.1 nm. The typical emission spectra acquired in Ar-Ti HiPIMS discharge at the end of plasma on time are presented in Figure 7. From the general emission spectrum (Figure 7(a)), the relevant spectral

regions containing Ti and Ti⁺ emission lines are visible (Figure 7(b–d)). The representative emission lines used in this work for resonant absorption are marked by arrows (see also Table 2). In most cases, the studied emission lines are well-resolved from the neighboring peaks. Due to this fast, rather low spectral resolution is normally sufficient for ROAS measurements. The total procedure for the number density determination consisted of the emission peaks intensities measurements (I_S, I_P, and I_{PS} values at each condition), A_L value determination by Eq. (4), determination of the absorption coefficient k_0 as a result of solving Eq. (3), followed by calculation of the absolute density of absorbers according to Eq. (1).
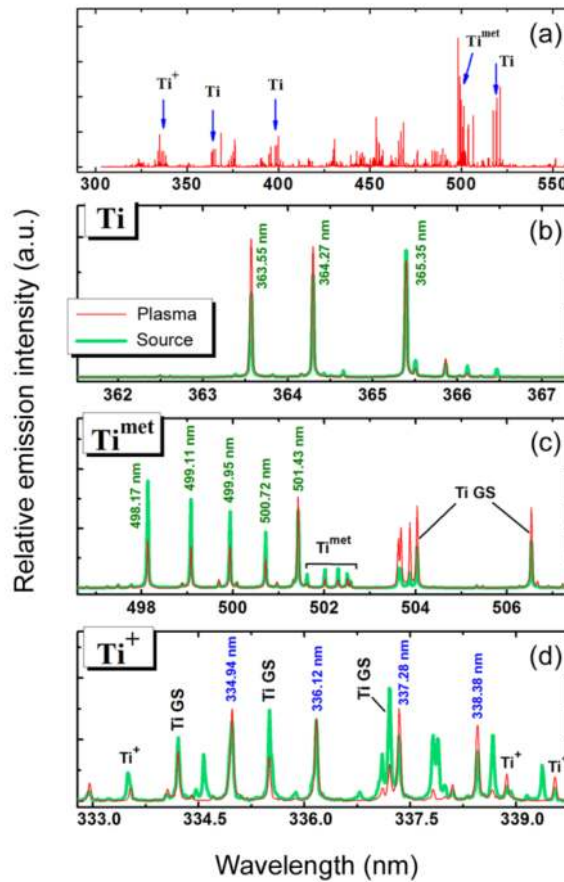

Figure 7. General emission spectrum (a) obtained in Ar-Ti HiPIMS discharge showing the spectral regions of interest used for the determination of the absolute density of different atomic species. The spectral regions corresponding to Ti ground state atoms (b), Ti metastables (c), as well as Ti ions (d) are shown separately. The HiPIMS and HCL spectra (b–d) are normalized arbitrary. Reproduced with permission from Britun et al. [38]. Copyright 2015 AIP Publishing.

Spectral parameter Studied atom	Nature of the probed state	Energy of the probed state (eV)	Emission wavelength λ (nm)	Spectral transition (lower–upper level, j–i)	Statistical weight of the lower level, g_j	Oscillator strength, f_{ji}[a]
Ti	Ground	0.000	363.55	$3d\,^2 4s\,^2$ a^{3}F$_2$–$3d\,^2(^3$F$)4s4p(^1$P°$)$ y^{3}G°$_3$	5	0.20
		0.021	364.27	$3d\,^2 4s\,^2$ a^{3}F$_3$–$3d\,^2(^3$F$)4s4p(^1$P°$)$ y^{3}G$_4$	7	0.16
		0.048	365.35	$3d\,^2 4s\,^2$ a^{3}F$_4$–$3d\,^2(^3$F$)4s4p(^1$P°$)$ y^{3}G$_5$	9	0.14
Ti^{met}	Metastable	0.813	501.43	$3d\,^3(^4$F$)4s$ a^{5}F$_1$–$3d\,^3(^4$F$)4p$ y^{5}G°$_2$	3	0.38
		0.818	500.72	$3d\,^3(^4$F$)4s$ a^{5}F$_2$–$3d\,^3(^4$F$)4p$ y^{5}G°$_3$	5	0.26
		0.826	499.95	$3d\,^3(^4$F$)4s$ a^{5}F$_3$–$3d\,^3(^4$F$)4p$ y^{5}G°$_4$	7	0.22
		0.836	499.11	$3d\,^3(^4$F$)4s$ a^{5}F$_4$–$3d\,^3(^4$F$)4p$ y^{5}G°$_5$	9	0.17
		0.848	498.17	$3d\,^3(^4$F$)4s$ a^{5}F$_5$–$3d\,^3(^4$F$)4p$ y^{5}G°$_6$	11	0.22
Ti$^+$	Ground	0.000	338.38	$3d\,^2(^3$F$)4s$ a^{4}F$_{3/2}$–$3d\,^2(^3$F$)4p$ z^{4}G°$_{5/2}$	4	0.28
		0.012	337.28	$3d\,^2(^3$F$)4s$ a^{4}F$_{5/2}$–$3d\,^2(^3$F$)4p$ z^{4}G°7/2	6	0.25
		0.028	336.12	$3d\,^2(^3$F$)4s$ a^{4}F7/2–$3d\,^2(^3$F$)4p$ z^{4}G°9/2	8	0.26
		0.049	334.94	$3d\,^2(^3$F$)4s$ a^{4}F9/2–$3d\,^2(^3$F$)4p$ z^{4}G °11/2	10	0.27
Ti^{+met}	Metastable	0.574	376.13	$3d\,^2(^3$F$)4s$ a^{2}F$_{5/2}$–$3d\,^2(^3$F$)4p$ z^{2}F°$_{5/2}$	6	0.22
		0.607	375.93	$3d\,^2(^3$F$)4s$ a^{2}F$_{7/2}$–$3d\,^2(^3$F$)4p$ z^{2}F°$_{7/2}$	8	0.21
Ar^{met}	Metastable	11.548	811.53	$3s\,^2 3p\,^5 4s(1s_5)$–$3p\,^5 4p(2p_9)$b	5	0.51
		11.723	794.82	$3s23p54s(1s_3)$–$3p54p(2p_4)$b	1	0.56

[a]The values of the oscillator strength are taken from Crintea et al. [75] for Ar and Wiese and Fuhr [76] otherwise.

[b]Paschen notations are used for Ar energy levels [75].

Table 2. Spectral parameters of the optical transitions for Ti, Ti^{met}, Ti$^+$, and Ar^{met} atomic states used in this work for ROAS diagnostics. Spectroscopic data are taken from the online NIST spectral database [74] unless stated otherwise. Reproduced with permission from Britun et al. [38]. Copyright 2015 AIP Publishing.

3. Particle density behavior in DCMS discharges

3.1. Spatial characterization of the DCMS discharge

Even though the main plasma parameters of the DCMS discharges do not alter in time, the plasma density as well as the density of the sputtered species may vary significantly as a function of the spatial position in the discharge. The first parameter in this case defines mainly the excitation level of the bulk and sputtered species as well as their ionization degree, whereas the (ground state) density of the sputtered species is mainly affected by the applied power, sputtering yield, target size, diffusion processes in the discharge volume, as well as by the other processes. The effects of ground state density depletion also may take place, as recently shown for DCMS discharges by LIF [49], but these effects are rather minor, especially com-

paring with HiPIMS case [37,38], since the ionization degree in the DCMS discharges generally remains at the level of few percent [15].

The optical diagnostics applied to a DCMS discharge clearly visualizes the plasma region corresponding to the confined electrons, which is represented by the bright area near the target surface observable by a naked eye, as shown in Figure 8. This region clearly corresponds to a spatial segment formed by the magnetic lines in the target vicinity, as shown in Figure 8(b), where the simulated magnetron magnetic field lines are drawn. The target diameter in this case is equal to 5 cm, but nevertheless the obtained data can be compared to the typical absolute density measured with larger targets (see Table 1), as soon as the target materials are the same and the current density are known, due to the scalability of the magnetron discharges [15]. In addition to this, as shown by Britun et al. [34], the emission lines in the plasma region decay exponentially along z direction, where an exponential dependence with significantly lower decrement is found at higher z, which corresponds to the diffusion region.
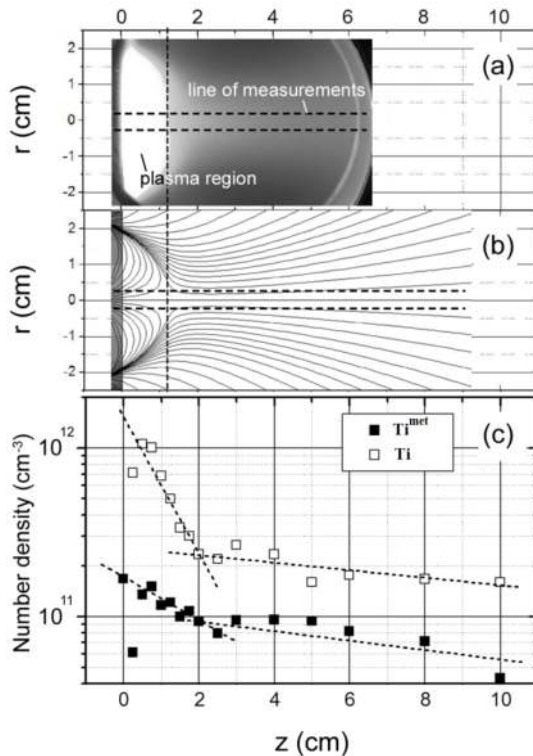

Figure 8. A photograph of the actual DCMS discharge operating at 4 mTorr of Ar pressure (a) along with the simulated magnetic field lines (b), and the distribution of the absolute density of Ti ground state atoms and Ti metastables measured by ROAS as a function of z at 30 mTorr of Ar pressure (c). Reproduced with permission from Britun et al. [34]. Copyright 2006 IOP Publishing.

In addition, the ground state density of the sputtered Ti as well as Ti metastables, measured by ROAS, follows the trend found for the emission lines by Britun et al. [34], as shown in Figure 8(c). As one can observe, the number density of Ti neutrals reaches nearly 10^{12} cm^{-3} near the target at the examined conditions (see Table 1), dropping about 5 times already at $z = 2$ cm, which is mainly due to the diffusion and the angular particularities of sputtering [50]. The Ti metastable atoms (the energy level is about 0.8 eV, see Table 2) reveal the same tendency having the total density 2–5 times smaller. The presented absolute values of Ti density are in the good agreement with related measurements performed in DCMS under the similar conditions [31]. We have to note that the found particularities of spatial distribution for the sputtered particles in DCMS should resemble those for HiPIMS discharges, as far as the magnetic field topology and the average power are similar. In HiPIMS discharge, however, the additional physical effects, such as the time-dependent broadening of the emission [22] and absorption spectral lines [44], cross-field ion transport [15,51], ionization-induced density depletion near the target [37], time-dependent current-induced changes of the magnetic field [52], etc., may not allow a direct comparison between the DCMS and the HiPIMS discharges in terms of the absolute density of particles. These differences should be even more essential with increasing of the plasma density, i.e., the magnetron current density, as briefly mentioned below.

3.2. Absolute density in reactive DCMS discharge

Another interesting possibility that ROAS provides is visualization and control of the physical processes during the so-called reactive sputtering. This process is mainly known for synthesis of oxide, nitride, and oxynitride thin films [21,53]. Reactive sputtering normally involves standard magnetron sputtering sources, where a certain percentage of, e.g., molecular oxygen or nitrogen, is added to the bulk gas (typically Ar) in order to finally synthesize oxide or nitride compounds. Physically, during the reactive sputtering, oxidation (nitriding, etc.) of the cathode superficial layer takes place, which is often referred to as "poisoned" regime. This process is characterized by a significant drop of the density of metallic species in the discharge volume [54]. Apart from this, a hysteresis effect (in terms of discharge voltage or metal atom density) depending on the direction of change of the reactive gas content is often considered to be among the main characteristics of reactive sputtering [15,55–57].

The example of measurements of the absolute number density of Ti atoms sputtered in a DCMS discharge at $z = 8$ cm away from the target using resonant absorption is given in Figure 9. Molecular nitrogen has been added to the bulk gas in this case in order to synthesize nitride films, as described in details in [54]. As we can see, as a result of nitrogen addition, a clear drop in the density of the metal (Ti) atoms can be detected. Due to the target poisoning, the density of sputtered Ti drops by a factor of about 4 when the nitrogen content in the discharge exceeds ≈5%. The relative density of Ti ions in this case is measured using mass-spectrometry, demonstrating the same effect. Based on this example, we can conclude that the (real-time) measurements of the absolute density using absorption spectroscopy, contrary to the well-known plasma emission monitoring method [58], may have additional benefits for reactive sputtering since the emission is always defined by electron excitation and may be weak at the high distances from the target. In addition, the spatial selectivity of ROAS may also be better

than that of OES, since the collimated beam used in this case can be highly focalized and thin, especially if a laser is used as a reference source [27].
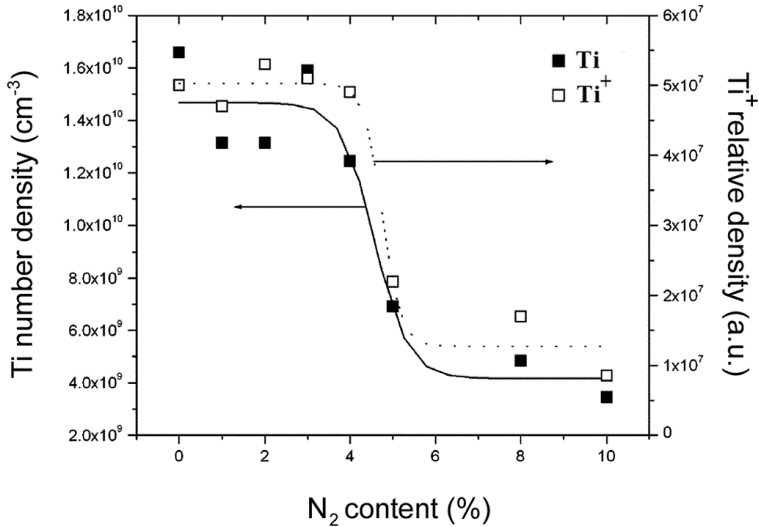

Figure 9. Evolution of the absolute Ti ground state density measured by ROAS (filled squares) and Ti+ relative density obtained by mass spectrometry (open squares) in a reactive DCMS discharge as a function of the nitrogen content. Ar pressure = 30 mTorr, applied power = 500 W, z = 8 cm. Reproduced with permission from Konstantinidis et al. [54]. Copyright 2005 Elsevier Publishing.

4. Particle density dynamics in HiPIMS discharges

HiPIMS discharges, possessing very short plasma on time, as illustrated in Figure 2, demonstrate different physics from that known for the DCMS discharges. The main reason for this is significantly elevated plasma density as well as the ionization degree related to both the bulk gas and the sputtered particles in HiPIMS, as mentioned in the Introduction and analyzed in the numerous works. Despite the fact that DCMS and HiPIMS sputtering processes can be realized using the same magnetron source, the direct comparison between these discharges is rather difficult, especially at the high values of the peak power applied to HiPIMS (or cathode current density), even though the time-averaged level of the applied power might be the same. In this section, for the sake of illustration of the dynamics of HiPIMS discharge in terms of the absolute density of species, the time-resolved evolution of the main discharge species in an Ar-Ti short-pulsed HiPIMS discharge analyzed by ROAS is presented. The experimental details on the HiPIMS system used for diagnostics are listed in Table 1, whereas the corresponding spectroscopic data are available in Table 2, or can be found elsewhere [31,38].

4.1. Time-resolved particle density evolution in HiPIMS

The time-resolved evolution of the absolute densities of Ti and Ti⁺ atomic species sputtered in a 20-μs pulse Ar-Ti HiPIMS discharge measured at $z = 5$ cm above the target is shown in Figure 10. The total density in this case represents the sum of populations of the corresponding ground state sublevels (see Table 2). As we can observe from this figure, after a small density decrease (depletion) during the plasma on time, the Ti density is peaking at the time delay $\Delta t \approx 100$ μs and reaches the value of about 6×10^{11} cm^{-3}. The number density is found to be proportional to the pulse duration in this case, as far as the other discharge parameters are the same, which should be due to the change in the pulse energy (0.13 vs. 0.26 J). The pulse duration effect is also valid for the Ti ions in HiPIMS (not shown). The decrease in Ti density at the end of the plasma on time (roughly twice) is likely related to the VDF broadening of the sputtered particles during this time, neglected during the density calculation, as explained in [38]. In this case, an increase in the VDF width during the plasma on time observed by Palmucci et al. [44] results only in ~20% of the total density drop, which is less than the depletion visible in Figure 10(a) for Ti. This implies a presence of the additional factors responsible for density depletion, such as ionization of the sputtered particles, as discussed by Britun et al. [37]. Quantitative estimation of the different contributions is barely possible in this case, primarily due to the strong plasma emission in this time interval, which results in high deviation of the obtained data. The error bar shown in Figure 7(a) represents a standard deviation of the data points corresponding to several independent ROAS measurements, whereas the density data correspond to the values averaged among several measurements, as well as among three Ti ground state energy sublevels listed in Table 1.
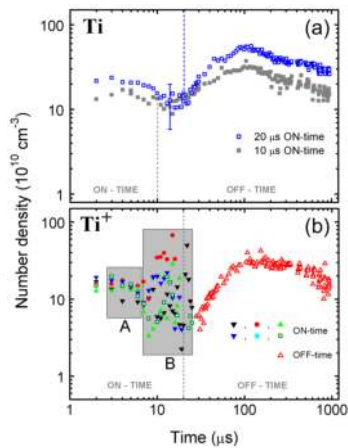

Figure 10. Time-resolved evolution of the Ti (a) and Ti⁺ (b) number density in Ar-Ti HiPIMS discharge measured by ROAS. The A and B time intervals correspond to the density depletion and the current self-organization, respectively. Six independent measurements have been undertaken in the case of Ti⁺ continuously showing the density instabilities in the interval B. Ar pressure = 20 mTorr, $z = 5$ cm. Reproduced with permission from Britun et al. [38]. Copyright 2015 AIP Publishing.

The evolution of the Ti ion density shown in Figure 10(b) reveals similar tendencies, especially during the plasma off time, where the density has a maximum at 100–200 μs, reaching ~3 × 10^{11} cm^{-3}. During the plasma on time, two phenomena can be observed: the first one is the beginning of density depletion interval, which is similar to that found for Ti neutrals (called interval A), and the second one which characterized by the strong instabilities of the measured Ti$^+$ density at the end of the plasma on time, resembling the stochastic density behavior (called interval B). Note that six independent density measurements made during the plasma on time always lead to the different Ti$^+$ density evolution. Since Ti ionization is likely defined by the electrons presented in the discharge volume during this time ($Ti + e \rightarrow Ti^+ + 2e$), the latter phenomenon is probably related to the discharge current self-organization at the end of the plasma on time, resulting in a nonperiodic rotation of the excitation zones ("spokes") along the target race-track area, as reported by Kozyrev et al. [59] and studied by the other groups [60–62]. Apparently, the uncertainties in the measured Ti$^+$ density during the interval B persist even after the averaging of the signal over 10^3 pulses by the ICCD detector. This implies an existence of the additional factors responsible for the strong uncertainty of Ti$^+$ density, such as the high plasma-to-source emission peak ratio at the end of plasma on time. Indeed, a strong domination of the plasma emission intensity over the emission from the reference source dramatically decreases the stability of ROAS measurements. In our case, the typical emission intensity from plasma may surpass the one coming from the reference source by a factor of about 100 for Ti ions, and of about 30 for Ti neutrals, as illustrated in Figure 11. As follows from the recent analysis performed by Britun et al. [48], the relative error of the ROAS measurements in this case may easily exceed 100%, even if the relative error of the emission intensity measurements is only about 5% (typical for ICCD detectors), which may explain the instabilities observed during the HiPIMS on time for ions. Because of the mentioned instabilities, the plasma parameters such as Ti ionization degree, which can be defined for Ti as

$$\eta = \frac{\left[Ti^+ \right]}{\left[Ti^+ \right] + \left[Ti \right]} \tag{5}$$

(where $[X]$ stand for the absolute number density of specie X), are rather difficult to determine during the interval B. In the plasma off time, however, η reaches the level of about 0.4, which is typical for HiPIMS off time [63], taking into account rather low pulse energy used in this work (E_P = 0.26 J).

The summary of the time evolution of several atomic species studied in a 20-μs Ar-Ti HiPIMS discharge at $z = 5$ cm is given in Figure 12. From this figure, the main stages of HiPIMS discharge can be distinguished. First, after the discharge ignition, the excitation of Ar and Ti atoms remaining from the previous plasma pulse is taking place, as a result of propagation of the secondary electrons away from the cathode. The background Ti density is found to be ~2 × 10^{11} cm^{-3}, whereas the density of Ti metastables is much lower (~10^{10} cm^{-3}) for the considered conditions. The propagation of the hot electrons [64,65] results in formation of the Ar and Ti metastable states (Ar^{met}, Ti^{met}) as well as in the intensive Ti ionization during the plasma on
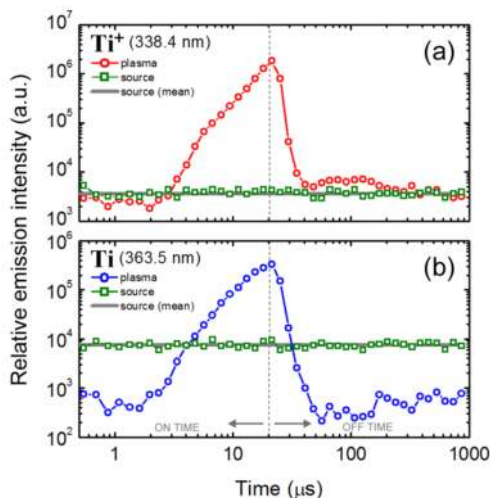
Figure 11. Typical example of the time evolution of Ti+ (a) and Ti (b) emission line intensity in Ar-Ti HiPIMS discharge comparing to the intensity of the same emission lines in the reference source (HCL) showing a dramatic increase in the emission intensity at the end of the HiPIMS pulse. Ar pressure = 20 mTorr, z ~1 cm.
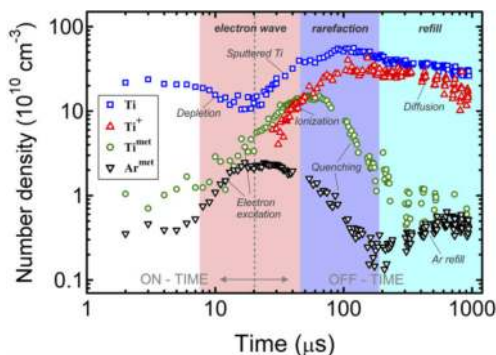

Figure 12. Summary of time evolution of the absolute density corresponding to the main discharge species in Ar-Ti HiPIMS discharge measured by ROAS. Three main time intervals corresponding to the secondary electron wave propagation, rarefaction, and refill are indicated. Ar pressure = 20 mTorr, z = 5 cm. Reproduced with permission from Britun et al. [21] (Copyright 2014 IOP Publishing) and Britun et al. [22] (Copyright 2015 WILEY-VCH Publishing).

time–beginning of the plasma off time, which is accompanied by the inversion of population of the Ti energy sublevels, as discussed below. At the beginning of the plasma off time, the density of metal ions increases (red triangles in Figure 12), corresponding to their transport toward the volume analyzed by ROAS. Second, the depletion of Ti density at the end of the plasma on time is also visible. This depletion can be induced by the VDF broadening of Ti neutrals at the end of the plasma pulse [44]. Apart from this, a strong ionization of the sputtered neutrals in this region should also contribute to the observed density depletion [37,38]. Third,

the strong excitation and ionization above the target are followed by rarefication of the bulk gas, resulted by the sputtered Ti species incoming to the studied volume, which is clearly observable together with a decrease in the Ar^{met} density, and also supported by the recent 2D density mapping results [37]. This process should be accompanied by electron cooling, as a result of collisions with the incoming heavy particles [64]. The ionization of sputtered Ti is taking place during the same time interval (20–100 μs), presumably as a result of the direct electron impact ($Ti + e \rightarrow Ti^+ + 2e$). The role of Penning ionization of Ti ($Ti + Ar^{met} \rightarrow Ti^+ + Ar + e$) in this case is supposed to be negligible, due to the much higher measured increase in Ti^+ density ($\Delta[Ti^+] \approx 2 \times 10^{11}$ cm^{-3}) comparing to a small decrease in the density of Ar^{met} ($\Delta[Ar^{met}] \approx 2 \times 10^{10}$ cm^{-3}) during this time. Finally, in addition to the gas rarefication above the target, the quenching of both Ti and Ar metastable states by the sputtered Ti should also contribute in the observable decrease of Ti^{met} and Ar^{met} density during the 50- to 200-μs time interval. Afterward (at $\Delta t > 200$ μs), the refill of Ar to this area is observed, which is consistent with the Ar refill time estimated in the related works [26,66]. The Ti and Ti^+ ground state densities gradually decrease during this time, due mainly to the diffusion of these species. The described processes are summarized in Table 3 where the main kinetic reactions along with the possible reasons for the observed processes are given.

Time	Particle	Processes	Main reaction(s)	Evidence
	Electrons	Generation		
	Ar	Ionization + acceleration toward the cathode	$Ar + e \rightarrow Ar^+ + 2e$	Related works [15]
0–5 μs	Ti	————		
	Ti^{met}	Have their "background" density level, remaining from previous plasma pulse.		
	Ti^+	————		
	Electrons	**Electron wave** propagation (secondary hot electrons—e^{sec}) (few km/s)		LIF imaging data [37], Langmuir probe measurements [77]
	Ar^{met}	Generation by e^{sec}	$Ar + e \rightarrow Ar^{met} + e$	LIF imaging data [37]
5–20 μs	Ti	VDF broadening and strong ionization, resulting in density depletion		LIF imaging data [37], measured VDF width [44]
	Ti^{met}	Generation by e^{sec}	$Ti + e \rightarrow Ti^{met} + e$	Presence of Ar^{met} during this interval [37]
	Ti^+	Generation by e^{sec} (?)	$Ti + e \rightarrow Ti^+ + 2e$	Not visible, probably due to the discharge current instabilities [59,60]
20–50 μs	Electrons	**Electron wave** (gradual cooling)		LIF imaging data [37], inversion of sublevel populations [67] (Figures 13 and 14).

Time	Particle	Processes	Main reaction(s)	Evidence
	Ar^{met}	1. Saturation, rarefication 2. Quenching by incoming Ti neutrals	2. $Ar^{met} + Ti \rightarrow Ar + Ti$	1. Decrease in $[Ar^{met}]$, Related studies [15,26] 2. LIF imaging data [37]
	Ti	1. Propagation of sputtered Ti 2. Ti VDF relaxation		1. LIF imaging data [37] 2. Related studies [44,45]
	Ti^{met}	Follow the growth of [Ti]	$Ti + e \rightarrow Ti^{met} + e$	Same growth rate for Ti and Ti^{met} (Figure 12)
	Ti^{+}	Generation (following Ti wave)	1. $Ti + e \rightarrow Ti^{+} + 2e$ 2. $Ar^{met} + Ti \rightarrow Ti^{+} + Ar + e$ (Penning ionization)	1. Faster growth of $[Ti^{+}]$ and slower growth of [Ti] at the same time 2. Negligible, due to very small drop in $[Ar^{met}]$ (Figure 12)
50–200 μs	Electrons	Thermalization	$X + e^{\,hot} \rightarrow X + e^{\,cold}$, where X is mainly Ti	Loss of the inversion of sublevel populations (Figure 14), Langmuir probe data [64,65], modeling [78]
	Ar^{met}	**Rarefication**		Figure 12
	Ti	Diffusion		Gradual decrease of [Ti] (Figure 12)
	Ti^{met}	Quenching, diffusion	$Ti^{met} + X \rightarrow Ti + X$, where X is a heavy particle	Permanent density drop, as well as $[Ti^{met}]/[Ti]$ ratio drop (Figure 12)
	Ti^{+}	Density saturation (production-loss balance)		Figure 12
200–1000 μs	Electrons	Thermalized		Related works [64,65,78]
	Ar^{met}	**Refill**		Increase in $[Ar^{met}]$, refill time estimations [26,66]
	Ti	Continuing diffusion		Gradual decrease of [Ti] (Figure 12)
	Ti^{met}	Reaching background $[Ti^{met}]$ level ~10^{10} cm^{-3}.		Figure 12
	Ti^{+}	Slight drop after 600 μs, might be due to:	1. $X^{+} + Ar + e \rightarrow X + Ar^{met}$ 2. $X^{+} + e \rightarrow X$ where $X = Ar, Ti$	1. $[Ti^{+}]$ drop + $[Ar^{met}]$ increase 2. $[Ti^{+}]$ drop (Figure 12)

Table 3. Summary of the processes related to the absolute density evolution of the discharge species measured by ROAS in a 20-μs Ar-Ti HiPIMS discharge (see Figure 12). Partially reproduced with permission from Britun et al. [38]. Copyright 2015 AIP Publishing.

4.2. Inversion of the energy sublevel populations

An interesting effect can be observed if the measured density is represented separately for each energy sublevel at the studied electronic state, as shown in Figure 13. As one can observe, a clear inversion among the studied energy states is achieved for five Ti sublevels corresponding to the metastable Ti a^5F_J states (see Table 2). An inversion of the considered energy sublevels (i.e., when the population of the state corresponding to higher energy is found to be higher) takes place in Figure 13(a) during the 20- to 100-µs time interval. The maximum of the mentioned inversion for Ti^{met} case is located around $\Delta t \approx 60$ µs. Similar but much weaker effect for Ar metastables (only two levels are considered) is also visible in Figure 13(b).
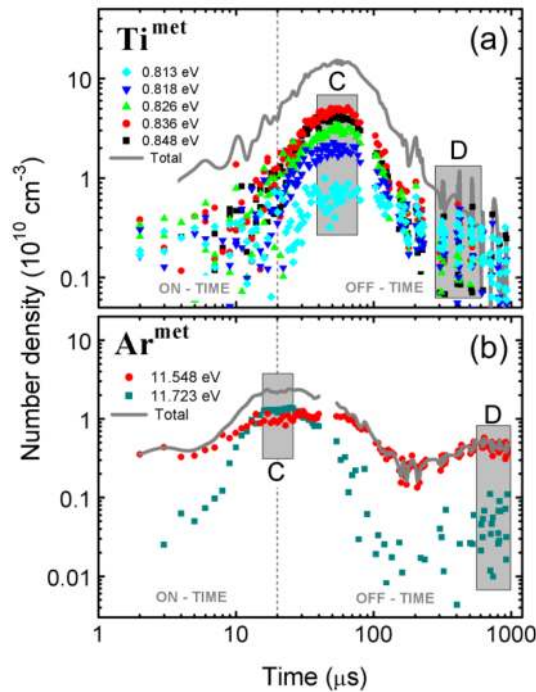

Figure 13. Time-resolved number density evolution for Ti (a) and Ar (b) metastable atoms measured by ROAS in Ar-Ti HiPIMS showing the populations of the corresponding energy sublevels (see Table 2). The total density evolution is given by gray lines for comparison. Ar pressure = 20 mTorr, z = 5 cm. Reproduced with permission from Britun et al. [38]. Copyright 2015 AIP Publishing.

Despite the fact that the inversion effect is rather new for HiPIMS, it is well known for the other low-temperature discharges, such as Ti hollow cathode plasma [67], and RF-amplified DCMS discharge [30]. In the former case, it is explained by the (partial) equilibrium of the heavy discharge species with the energetic electrons during the short plasma on time interval. Besides this, the inversion of the sublevel populations might be also responsible for the apparent density depletion in the magnetron target vicinity detected in the DCMS discharges

[30,49,68,69]. The sublevel inversion can be explained based on the Boltzmann distribution of the corresponding energy sublevel populations. Assuming the presence of the dense flux of hot electrons during certain time in the discharge, the heavy particles should be intensively excited by the electrons during this time. Under these conditions, for the close energy sublevels, the factor $\Delta E / kT$ in the Boltzmann distribution may be negligible due to rather high effective (excitation) temperature of the involved particles. This should result finally in the proportionality between the level population N_i and its statistical weight g_i, as shown by the following expressions:

$$\frac{N_i}{g_i} = \frac{N_j}{g_j} \cdot \mathrm{Exp}\left(-\frac{E_i - E_j}{kT_{exc}}\right) \equiv \frac{N_j}{g_j} \cdot \mathrm{Exp}\left(-\frac{\Delta E}{kT_{exc}}\right) \tag{6}$$

where i (upper) and j (lower) stand for two close levels, $N_{i,j}$ is the level populations, $g_{i,j}$ - is their statistical weights, ΔE is the energy difference between two levels, and T_{exc} is the excitation temperature. Under $\Delta E \ll kT_{exc}$, we obtain the following:

$$\frac{N_i}{g_i} \approx \frac{N_j}{g_j}\left(1 - \frac{\Delta E}{kT_{exc}}\right) \approx \frac{N_j}{g_j} \tag{7}$$

which, after normalization to $\frac{N_j}{g_j}$, results in $N_i \sim g_i$. Note that this effect has the same nature as the "saturated LIF" mode described by Amorim et al. [70].

The sublevel inversion is even more clear if a "stabilized" modification of the resonant absorption method is implemented, when a pulsed reference source is synchronized with the time gate of the ICCD detector, as discussed above. The relative error of the ROAS measurements can be significantly reduced in this case, and fine spectral effects in the discharge, such as inversion of the energy sublevels, can be easily visualized. The example of these measurements using three Ti ground state energy sublevels is given in Figure 14. In Figure 14(a), the experimental ROAS results, clearly showing the presence of the Ti ground state sublevel inversion (roughly between 20 and 300 μs), are shown. At the same time, a sketch of the same level populations drawn in accordance to the inversion model described by Eqs. (6) and (7) is given in Figure 14(b) for the sake of clarification of the experimental data. We have to note that before the inversion interval, the studied Ti sublevels do not perfectly follow the Boltzmann distribution, as the middle level is mostly populated in this case. This fact might be due to the complicated HiPIMS discharge kinetics, which is not well studied yet. Let us also note that the inversion interval might be significantly shifted in time depending on position of the ROAS line of sight, and the inversion should happen much earlier if the measurements are performed closer to the target surface.
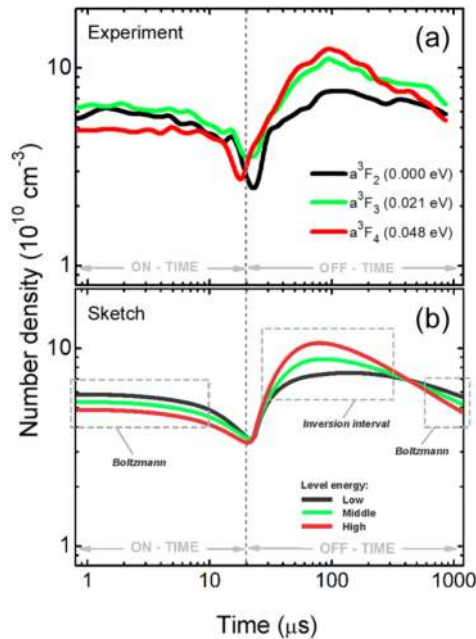
Figure 14. The time-resolved populations of three ground state Ti energy sublevels (a) measured in Ar-Ti HiPIMS discharge by ROAS using the dynamic source triggering. Ar pressure = 20 mTorr, z = 5 cm. A sketch (b) illustrating the dynamics of the Ti sublevels population as a function of time in HiPIMS. The beginning of the inversion interval should depend on the observation point (z) and should start earlier if the ROAS line-of-sight is located closer to the target.

Fitting the experimental data corresponding to Ti sublevels, the Ti *excitation* temperature can be obtained, which is a measure of excitation of the corresponding energy sublevels by the hot electrons. In our case, the estimations lead to T_{exc} ~0.25 eV for Ti, and to the close value for Ti^{met}. In general, a precise ROAS measurement of the energy sublevel populations for a certain atomic state should allow a reliable determination of the excitation temperature T_{exc} for the heavy discharge particles after their interaction with hot electrons, as well as the determination of its temporal evolution in the discharge. Representing a measure of excitation of the heavy particles by electrons in the discharge volume, T_{exc} should be proportional to the HiPIMS pulse energy, secondary electron emission coefficient, and should be generally higher in the target vicinity [22].

4.3. Density dynamics in reactive HiPIMS

It is also interesting to consider some selected phenomena in the case of reactive HiPIMS discharge. The behavior of the number density of the sputtered species in reactive HiPIMS should follow the same tendency as in the reactive DCMS case (shown in Figure 9), i.e., a density drop by several times in the poisoned regime of sputtering should be expected. Let us

consider the behavior of the absolute density of *reactive* species here. The presented example is related to the time-behavior of the absolute density of the atomic oxygen measured by ROAS. This question has been particularly studied by Vitelaru et al. [71] using a tunable diode laser and giving the dynamics of the atomic oxygen in the HiPIMS discharge, however, without measuring its absolute density, which is a very important parameter, as mentioned in Section 1. In the considered case, a discharge-based ROAS with simultaneous signal acquisition (see Figure 6) has been applied for measurements of the absolute density of O atoms in the HiPIMS discharge volume. Due to the spectral limitations, however, the ground state O atoms are not accessible by ROAS (the corresponding transitions are located in the deep UV range [72]), so only the O *metastable* atoms (O^{met}, 3s $^5S°_2$ level with the energy = 9.15 eV) are analyzed in this case. A microwave surfaguide discharge [73] operating at 2.5 GHz and using Ar–7% O_2 gas mixture has been utilized as a reference source in this case.

Analyzing the O^{met} atoms in any discharge, one should bear in mind that these are excited species which keep the dynamics of the plasma electrons as well as the dynamics of the ground state O_2 and O. The time evolution of O^{met} atoms measured by ROAS at $z = 5$ cm in the HiPIMS discharges working with Ar–20% O_2 gas mixture and using Ti and Ag targets is shown in Figure 15. The typical stages of nonreactive sputtering discharge can be observed in this case (compare to Figure 12). The first noticeable processes are the O^{met} density depletion at the beginning of the plasma on time (visible in the Ti target case only) followed by the density increase at the end of the plasma on time. These processes are followed by the rarefication of O^{met} and the gas refill afterward (exists both for Ti and Ag target cases). We would like to emphasize that both in Ti and Ag cases the O^{met} density starts to increase already at the end of the plasma on time, unlike in the nonreactive case. Such an increase correlates well with the time-resolved dynamics of the Ar metastables in the nonreactive case, as shown in Figure 12. This similarity, as well as the proximity of the excitation thresholds for these species (11.55 eV for Ar^{met} vs. 9.15 eV for O^{met} [74]) point out on the role of the secondary electrons in formation of the O^{met} state, which should take place already during the plasma on time (i.e., $O_2 + e \rightarrow O + O + e$, followed by $O + e \rightarrow O^{met} + e$). The correlation with Ar^{met} is additionally confirmed by the gas rarefication and refill processes observed both for Ar and atomic O during the plasma off time. The different density values in the density maxima of O^{met} ($\approx 5 \times 10^8$ cm^{-3} for Ti vs. $\approx 3 \times 10^9$ cm^{-3} for Ag) may be related to the differences in the ion-induced secondary electron emission (ISEE) coefficients in these cases, assuming the electron impact to be a primary mechanism for O^{met} formation. Interestingly, the absolute number density below 10^8 cm^{-3} has been detected in these measurements, approving the high reliability of ROAS with simultaneous signal detection. (see Figure 6).

Since in the case of Ar–20% O_2 gas mixture magnetron target is supposed to be completely oxidized [47], the sputtering of oxide material from (i.e., M_xO_y molecules, where M is a metal atom) followed by formation of O atoms and finally O^{met} should be another possible mechanism of the observed O^{met} density elevation at the end of the plasma on time. This mechanism, however, is supposed to be rather minor since the wave of the sputtered species arrives in the volume of measurements much later, having the maximum at $\Delta t \approx 100$ μs, as shown in Figure 12.
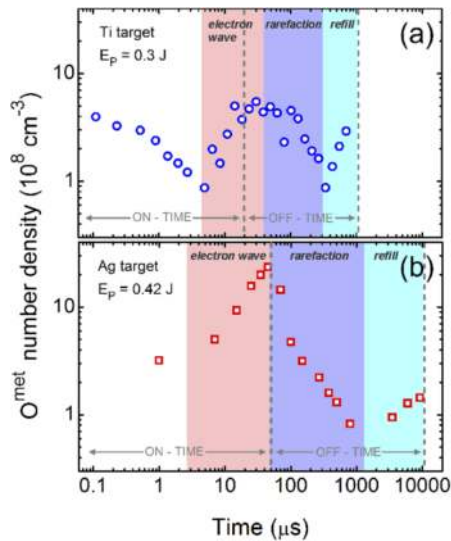
Figure 15. Time-resolved evolution of the absolute density of O metastable atoms (3s 5S$^0_2$ state) measured by ROAS in HiPIMS discharge using Ar–20% O$_2$ gas mixture for the case of Ti (a) and Ag (b) cathode. Ar pressure = 20 mTorr, z = 5 cm. Pulse duration, discharge frequency, and pulse energy (E_P) are, respectively, 20 ms, 1 kHz, 0.3 J (a) and 50 ms, 0.1 kHz, 0.42 J (b). Reproduced with permission from Britun et al. [22]. Copyright 2015 WILEY-VCH Publishing.

5. Summary and conclusions

5.1. DCMS discharges

Resonant absorption analysis of the direct current sputtering discharges shows that the absolute density of the sputtered particles is ranged in a relatively narrow interval, being always in the range of 10^{10}–10^{12} cm^{-3} in the Ti case (assuming the average power level to be several hundred Watt). These values may be somewhat different varying the cathode materials with essentially different sputtering yield and/or in the sputtering systems, which use significantly higher power levels. The spatial distribution of the sputtered particles is mainly determined by their diffusion (at high pressure), by the angular directivity of sputtering (low pressure), as well as by the magnetic field topology (critical mainly for the sputtered ions), which lead to nearly exponential decay of the observed density of species as a function of the distance from cathode, so the density might decay at least by one order of magnitude already at few cm away from the target surface (for 5 cm diameter round target).

One of the advantages of using ROAS technique for diagnostics of sputtering processes is its ability to probe the species in a wide range of absolute density, starting from roughly 10^7–10^8 cm^{-3}, where the signal-to-noise ratio of the used detector is a limiting factor, and finishing by the values several orders of magnitude higher, when the increase of the optical thickness of the volume of interest becomes the limiting factor. The bottom sensitivity level may be additionally affected by the type of the absorption scheme used (e.g., single-pass, multipass,

with or without simultaneous signal acquisition, etc.). The variety of the ROAS implementation schemes allow real time monitoring of the sputtered species also during *reactive* sputtering, which is very demandable, as the synthesis of the compound (oxides, nitrides, etc.) coatings is one of the main sputtering workflow nowadays. Since the density drop between the "metallic" and "reactive" mode of sputtering normally drop by about one order of magnitude, the absolute density levels in both modes can be easily real time monitored by absorption technique, which might be useful for research-oriented as well as for industry applications. This conclusion is valid both for DCMS (as shown in this work), pulsed-DC, as well as for HiPIMS discharges.

5.2. HiPIMS discharges

The physical phenomena in the HiPIMS discharges are rather different from those observed in DCMS and P-DCMS cases, first of all in terms of the plasma density and much shorter timing (μs scale). As a result, numerous dynamic effects should be taken into account explaining the properties of the HiPIMS discharges. Among these effects, the following time-dependent phenomena should be mentioned: the propagation of the fast electron wave the dynamic gas rarefaction and refill, the ionization and excitation of various discharge particles, quenching of the excited states as a result of collisions, the anomalous electron transport, etc. ROAS technique, being essentially limited by only the time-resolution of the used optical detector, suits very well for systematic characterization of these discharges in terms of the absolute density. In addition, the modern ICCD detectors typically provide ns time resolution, which surpasses the typical HiPIMS time scale by few orders of magnitude.

In terms of the time-resolved evolution of the discharge particles density, there are several processes in HiPIMS discharge, which can be visualized using ROAS technique. The time-resolved summary of these processes is given in Table 3, considering the main discharge species studied in the Ar-Ti nonreactive HiPIMS case. The presence of such dynamic effects as the density depletion, gas rarefaction, gas refill, quenching of the metastable states, ionization, as well as the propagation of the electron wave away from the target surface can be concluded based on the undertaken ROAS analysis. Despite a rather high HiPIMS repetition rate considered in this work (1 kHz), the gradual relaxation for the majority of the listed processes till the end of the plasma off time can be observed. Even though the total range of the measured absolute density of the discharge species reaches nearly three orders of magnitude in the considered case, the detected densities are still well above the detection threshold (which is estimated to be roughly 10^7–10^8 cm^{-3} with the detection scheme used). The sensitivity of the used ROAS method can be additionally enhanced using the lock-in detection technique, dynamic triggering of reference source, and related approaches.

One of these approaches, namely, the simultaneous acquisition of the emission signals using a triple optical fiber, has been utilized for time-resolved detection of the oxygen metastable atoms during the reactive HiPIMS process. The results reveal the presence of the same discharge phases (such as gas rarefaction and refill, as well as the density depletion in some cases) as detected in the nonreactive HiPIMS case. The absolute density of the O metastable atoms detected in this case is still above the mentioned ROAS sensitivity threshold, being in

the range of 10^8–10^9 cm^{-3}. The optical diagnostics of the reactive HiPIMS discharges, however, is a relatively new area and the obtained results require additional verification by the other methods, such as LIF, in order to be understood completely.

5.3. General remarks

The resonant absorption technique represents a powerful diagnostic tool suitable for the determination of the absolute density of the relevant species in sputtering discharges, such as DCMS, P-DCMS, HiPIMS, as well as the other types of magnetron discharges. This technique has several modifications allowing its optimization depending on the discharge geometry etc. For example, using a plasma discharge as a reference source, ROAS setup can be rather simple, requiring only the additional optics for reference source beam collimation, and (sometimes) additional synchronization between the source and the discharge of interest. Both direct current and pulsed reference sources can be used for resonant absorption purposes. In addition to this, in case a broad range spectral detector, such as ICCD, is utilized, a parallel detection of several spectral transitions as well as the corresponding absolute densities becomes possible. These advantages open new possibilities to study the basic effects in the discharge volume. Among these effects are the population of the metastable levels of the various discharge species, the population of the atomic energy sublevels of the atoms and their time-resolved dynamics, the study of the excitation temperature across the discharge volume, etc. These possibilities are important for studying magnetron sputtering processes at the fundamental level, whereas rather basic configuration of the ROAS setup may be helpful in industry, e.g., for real-time density monitoring of the relevant species during a certain process.

The sensitivity of the absorption method can also be significantly improved by varying the detection schemes, such as lock-in amplification (improving the sensitivity by 1–2 orders of magnitude typically), multipass methods, as well as by simultaneous signal acquisition, dynamic source triggering, etc. Using the simultaneous signal acquisition for example, the sensitivity below 10^8 cm^{-3} has been achieved for O metastable atoms in a reactive HiPIMS discharge case, as illustrated in this chapter. This value is far below the typical concentrations of the sputtered atoms in the discharge (10^{10}–10^{12} cm^{-3}) achieved under the laboratory conditions, which is enough for most applications. For very weakly populated energy states, like those appearing in molecular discharges, the multipass absorption, including the ring-down spectroscopy method, could be suggested, which are, being out of the scope of this chapter, still based on the same fundamental principles.

Acknowledgements

Author details

Nikolay Britun[1*], Stephanos Konstantinidis[1] and Rony Snyders[1,2]

*Address all correspondence to: nikolay.britun@umons.ac.be

1 Chimie des Interactions Plasma–Surface (ChIPS), CIRMAP, Université de Mons, Mons, Belgium

2 'Materia Nova' Research Center, Parc Initialis, Mons, Belgium

References

[1] S. M. Rossnagel, J. Vac. Sci. Technol. A. 21, S74 (2003).

[2] G. Bräuer, B. Szyszka, M. Vergöhl, and R. Bandorf, Vacuum 84, 1354 (2010).

[3] W. R. Grove, Philos. Trans. R. Soc. London 142, 87 (1852).

[4] P. Sigmund, *Sputtering by Particle Bombardment I. Physical Sputtering of Single-Element Solids* (Springer, Berlin, 1981).

[5] W. D. Gill and E. Kay, Rev. Sci. Instrum. 36, 277 (1965).

[6] E. Kay, J. Appl. Phys. 34, 760 (1963).

[7] J. S. Chapin., Res. Dev. 25, 37 (1974).

[8] R. D. Arnell and P. J. Kelly, Surf. Coat. Technol. 112, 170 (1999).

[9] P. J. Kelly and R. D. Arnell, Vacuum 56, 159 (2000).

[10] S. Schiller, K. Goedicke, J. Reschke, V. Kirchhoff, S. Schneider, and F. Milde, Surf. Coat. Technol. 61, 331 (1993).

[11] J. Musil, J. Lestina, J. Vlcek, and T. Tolg, J. Vac. Sci. Technol. A. 19, 420 (2001).

[12] U. Helmersson, M. Lattemann, J. Bohlmark, A. P. Ehiasarian, and J. T. Gudmundsson, Thin Solid Films 513, 1 (2006).

[13] S. M. Rossnagel and J. Hopwood, Appl. Phys. Lett. 63, 3285 (1993).

[14] A. Tonegawa, H. Taguchi, and K. Takayama, Nucl. Instrum. Methods Phys. Res. B. 55, 331 (1991).

[15] J. T. Gudmundsson, N. Brenning, D. Lundin, and U. Helmersson, J. Vac. Sci. Technol. A. 30, 030801 (2012).

[16] K. Sarakinos, J. Alami, and S. Konstantinidis, Surf. Coat. Technol. 204, 1661 (2010).

[17] J. T. Gudmundsson, Vacuum 84, 1360 (2010).

[18] I. K. Fetisov, A. A. Filippov, G. V. Khodachenko, D. V. Mozgrin, and A. A. Pisarev, Vacuum 53, 133 (1999).

[19] V. Kouznetsov, K. Macák, J. M. Schneider, U. Helmersson, and I. Petrov, Surf. Coat. Technol. 122, 290 (1999).

[20] U. Helmersson, M. Lattemann, J. Bohlmark, A. P. Ehiasarian, and J. T. Gudmundsson, Thin Solid Films 513, 1 (2006).

[21] N. Britun, T. Minea, S. Konstantinidis, and R. Snyders, J. Phys. D. Appl. Phys. 47, 224001 (2014).

[22] N. Britun, S. Konstantinidis, and R. Snyders, Plasma Process. Polym. DOI: 10.1002/ppap.201500051 (2015).

[23] K. Sarakinos, J. Alami, and S. Konstantinidis, Surf. Coat. Technol. 204, 1661 (2010).

[24] A. C. Mitchell and M. W. Zemansky, *Resonance Radiation and Excited Atoms* (Plenum Press, Cambridge, 1971).

[25] G. F. Kirkbright and M. Sargent, *Atomic Absorption and Fluorescence Spectroscopy* (Academic Press, London, 1974).

[26] C. Vitelaru, D. Lundin, G. D. Stancu, N. Brenning, J. Bretagne, and T. Minea, Plasma Sources Sci. Technol. 21, 025010 (2012).

[27] A. Zybin, J. Koch, H. D. Wizemann, J. Franzke, and K. Niemax, Spectrochim. Acta Part B At. Spectrosc. 60, 1 (2005).

[28] D. S. Baer and R. K. Hanson, J. Quant. Spectrosc. Radiat. Transf. 47, 455 (1992).

[29] L. De Poucques, J.-C. Imbert, C. Boisse-Laporte, J. Bretagne, M. Ganciu, L. Teulé-Gay, and M. Touzeau, Plasma Sources Sci. Technol. 15, 661 (2006).

[30] S. Konstantinidis, A. Ricard, M. Ganciu, J. P. Dauchot, C. Ranea, and M. Hecq, J. Appl. Phys. 95, 2900 (2004).

[31] M. Gaillard, N. Britun, Y. M. Kim, and J. G. Han, J. Phys. D. Appl. Phys. 40, 809 (2007).

[32] TOPTICA Photonics Webpage: http://www.toptica.com/products/research_grade_diode_lasers.html

[33] C. Vitelaru, L. de Poucques, T. M. Minea, and G. Popa, J. Appl. Phys. 109, 053307 (2011).

[34] N. Britun, M. Gaillard, L. Schwaederlé, Y. M. Kim, and J. G. Han, Plasma Sources Sci. Technol. 15, 790 (2006).

[35] N. Britun, S. Ershov, A.-A. El Mel, S. Konstantinidis, A. Ricard, and R. Snyders, J. Phys. D. Appl. Phys. 46, 175202 (2013).

[36] C. Vitelaru, L. de Poucques, T. M. Minea, and G. Popa, Plasma Sources Sci. Technol. 20, 045020 (2011).

[37] N. Britun, M. Palmucci, S. Konstantinidis, and R. Snyders, J. Appl. Phys. 117, 163302 (2015).

[38] N. Britun, M. Palmucci, S. Konstantinidis, and R. Snyders, J. Appl. Phys. 117, 163303 (2015).

[39] L. Li, A. Nikiforov, N. Britun, R. Snyders, and C. Leys, Spectrochim. Acta Part B At. Spectrosc. 107, 75 (2015).

[40] A. Ricard, V. Monna, and M. Mozetic, Surf. Coat. Technol. 174–175, 905 (2003).

[41] W. Lochte-Holtgreven, editor, *Plasma Diagnostics* (North-Holland publishing company, Amsterdam, 1968).

[42] N. Britun, J. G. Han, and S.-G. Oh, Plasma Sources Sci. Technol. 17, 045013 (2008).

[43] N. Britun, M. Palmucci, S. Konstantinidis, M. Gaillard, and R. Snyders, J. Appl. Phys. 114, 013301 (2013).

[44] M. Palmucci, N. Britun, S. Konstantinidis, and R. Snyders, J. Appl. Phys. 114, 113302 (2013).

[45] N. Britun, M. Palmucci, and R. Snyders, Appl. Phys. Lett. 99, 131504 (2011).

[46] M. Ganciu, M. Hecq, S. Konstantinidis, J.-P. Dauchot, M. Touzeau, L. de Poucques, and J. Bretagne, 2007/0034498 A1 (2007).

[47] M. Palmucci, N. Britun, T. Silva, R. Snyders, and S. Konstantinidis, J. Phys. D. Appl. Phys. 46, 215201 (2013).

[48] N. Britun, M. Michiels, and R. Snyders, Rev. Sci. Instrum. 86, (2015) In press.

[49] N. Britun, M. Gaillard, and J. G. Han, J. Phys. D. Appl. Phys. 41, 185201 (2008).

[50] A. Goehlich, D. Gillmann, and H. F. Döbele, Nucl. Instrum. Methods Phys. Res. B. 164–165, 834 (2000).

[51] D. Lundin, P. Larsson, E. Wallin, M. Lattemann, N. Brenning, and U. Helmersson, Plasma Sources Sci. Technol. 17, 035021 (2008).

[52] J. Bohlmark, U. Helmersson, M. VanZeeland, I. Axnäs, J. Alami, and N. Brenning, Plasma Sources Sci. Technol. 13, 654 (2004).

[53] J. Musil, P. Baroch, J. Vlček, K. H. Nam, and J. G. Han, Thin Solid Films 475, 208 (2005).

[54] S. Konstantinidis, A. Ricard, R. Snyders, H. Vandeparre, J. P. Dauchot, and M. Hecq, Surf. Coat. Technol. 200, 841 (2005).

[55] D. Depla, J. Haemers, G. Buyle, and R. De Gryse, J. Vac. Sci. Technol. A. 24, 934 (2006).

[56] M. Audronis and V. Bellido-Gonzalez, Thin Solid Films 518, 1962 (2010).

[57] D. Depla and S. Mahieu, editors, *Reactive Sputter Deposition* (Springer, 2008).

[58] P. P. Woskov, K. Hadidi, P. Thomas, K. Green, and G. Flores, Waste Manag. 20, 395 (2000).

[59] A. V. Kozyrev, N. S. Sochugov, K. V. Oskomov, A. N. Zakharov, and a. N. Odivanova, Plasma Phys. Rep. 37, 621 (2011).

[60] A. Hecimovic, M. Böke, and J. Winter, J. Phys. D. Appl. Phys. 47, 102003 (2014).

[61] A. P. Ehiasarian, A. Hecimovic, T. De Los Arcos, R. New, V. Schulz-Von Der Gathen, M. Boke, J. Winter, and M. Bke, Appl. Phys. Lett. 100, 114101 (2012).

[62] J. Andersson, P. Ni, and A. Anders, Appl. Phys. Lett. 103, 054104 (2013).

[63] A. Ehiasarian, A. Vetushka, A. Hecimovic, and S. Konstantinidis, J. Appl. Phys. 104, 083305 (2008).

[64] A. Pajdarová, J. Vlček, P. Kudláček, and J. Lukáš, Plasma Sources Sci. Technol. 18, 025008 (2009).

[65] P. Poolcharuansin and J. W. Bradley, Plasma Sources Sci. Technol. 19, 025010 (2010).

[66] D. Lundin, N. Brenning, D. Jädernäs, P. Larsson, E. Wallin, M. Lattemann, M. A. Raadu, and U. Helmersson, Plasma Sources Sci. Technol. 18, 045008 (2009).

[67] D. Ohebsian, N. Sadeghi, C. Trassy, and J. M. Mermet, Opt. Comm. 32, 81 (1980).

[68] N. Nafarizal, N. Takada, K. Shibagaki, K. Nakamura, Y. Sago, and K. Sasaki, Jpn. J. Appl. Phys. 44, L737 (2005).

[69] N. Nafarizal, N. Takada, and K. Sasaki, Jpn. J. Appl. Phys. 48, 126003 (2009).

[70] J. Amorim, G. Baravian, and J. Jolly, J. Phys. D. Appl. Phys. 33, R51 (2000).

[71] C. Vitelaru, D. Lundin, N. Brenning, and T. Minea, Appl. Phys. Lett. 103, 104105 (2013).

[72] R. Payling and P. Larkins, *Optical Emission Lines of the Elements (CD-ROM)* (Wiley & Sons Inc., New York, 2000).

[73] T. Godfroid, J. P. Dauchot, and M. Hecq, Surf. Coat. Technol. 174–175, 1276 (2003).

[74] NIST Atomic Spectra Database Lines Form: http://physics.nist.gov/PhysRefData/ASD/lines_form.html

[75] D. L. Crintea, U. Czarnetzki, S. Iordanova, I. Koleva, and D. Luggenhölscher, J. Phys. D. Appl. Phys. 42, 045208 (2009).

[76] W. L. Wiese and J. R. Fuhr, J. Phys. Chem. Ref. Data 4, 263 (1975).

[77] K. B. Gylfason, J. Alami, U. Helmersson, and J. T. Gudmundsson, J. Phys. D. Appl. Phys. 38, 3417 (2005).

[78] T. Kozák and A. Dagmar Pajdarova, J. Appl. Phys. 110, 103303 (2011).